Biosensors and Bioelectronics 124–125 (2019) 260–267

Contents lists available at ScienceDirect

Biosensors and Bioelectronics

journal homepage: www.elsevier.com/locate/bios

Simultaneous biosensing of catechol and hydroquinone *via* a truncated cube-shaped Au/PBA nanocomposite

Danfeng Jiang, Jun Pang, Qiannan You, Tao Liu, Zhenyu Chu*, Wanqin Jin*

State Key Laboratory of Materials-Oriented Chemical Engineering, College of Chemical Engineering, Nanjing Tech University, 5 Xinmofan Road, Nanjing 210009, PR China

ARTICLE INFO

Keywords:
Phenolic biosensor
Simultaneous testing
Truncated cube shape
Au/PBA nanocomposite

ABSTRACT

A simultaneous testing of the trace catechol (CC) and hydroquinone (HQ) was achieved *via* an ultrasensitive phenolic biosensor constructed by the truncated cube-shaped gold/Prussian blue analogue (Au/PBA) nanocomposites. A facile charge-assembly strategy was developed to drive the successive mutual attractions for the crystallization among $[Fe(CN)_6]^{3-}$, Co^{2+}, and $[AuCl_4]^-$ reactants, benefiting the *in-situ* growth of Au nanoparticles on all faces of the PBA truncated nanocubes. On account of this special architecture, numerous 10 nm Au particles can rapidly gather the electrons from the enzyme reaction to a PBA crystal due to their high conductivity, and then the current signals will be significantly magnified through the reversible redox of the PBA. Using this nanomaterial, the as-prepared biosensor has shown an extreme wide linear range (CC: 0.2–550 μM, HQ: 1–550 μM) and an ultralow detection limit (CC: 0.06 ± 0.001 μM, HQ: 0.3 ± 0.007 μM) for the independent detections of CC and HQ. More importantly, when the two targets coexist, this biosensor can simultaneously exhibit the obvious and accurate responses of CC and HQ at the different potentials (0.17 V for CC and 0.07 V for HQ) with the high sensitivities and rare mutually interferences.

1. Introduction

With the fast development of modern industry, the environment pollution is getting worse to severely threaten the organism health (Figueiredo et al., 2007). Among all kinds of pollutants, phenolic compounds are a typical category of high toxic and low degradable substances (Freire et al., 2002; Qaisar, Samuel, 2009; Wang et al., 2007), which are mainly leaked from industrial wastewater to lakes (Bensalah et al., 2005; Svitel, Miertus, 1998; Kaisheva et al., 1996). According to the International Agency for Research on Cancer, catechol (CC) and hydroquinone (HQ) are both listed as the possible human carcinogens. Currently, their testing method is generally based on the High Performance Liquid Chromatography (HPLC) for the practical water sample due to its high accuracy (Kanamori et al., 2016). However, too expensive cost, poor portability and long analysis period limit its application in the on-site and real-time detection (Karim et al., 2014).

In order to address above issues, the electrochemical biosensor is arousing more and more research interests for realizing the real-time catechol and hydroquinone detections (Lv et al., 2010). In the most phenolic biosensors, laccase is an important polyphenol oxidase for oxidizing the phenolic hydroxyl to produce the detection signal (Selvakumar et al., 2017; Melissa et al., 2015). However, the enzyme active center, flavin adenine dinucleotide (FAD), is deeply buried by proteins, causing the blocking of electron transfer (Wohlfahrt et al., 1999; Hitoshi et al., 2017). Hence, a high response signal is always a challenge for the accurate recognitions of the phenolic compounds. In this case, the design of an advanced material for bridging enzyme active center and electrode surface is a key to construct an ultrasensitive phenolic biosensor.

Prussian blue and its analogues are well-known as an electron mediator for the enzymatic reaction (Jiang et al., 2016; Chu et al., 2017; Arduini et al., 2015). Due to its reversible redox process produced by the metal center, they can transfer more electrons generated from the enzyme active center to the electrode surface, significantly magnifying the enzyme response signal to greatly improve the biosensing sensitivity and detection limit (Ho et al., 2004; Mattos and Gorton, 2001). In consideration of the semi-conductor nature of PBA materials, electrons are trouble to be excited from its valance band to conduction band. Therefore, its conductivity and electron transfer rate are both unsatisfactory for the electrochemical process (Chao et al., 2016; Jiang et al., 2017). To arouse the full advantages of PBA as a mediator, gold can be expected to compensate the defects in the electron transfer rate, especially reducing its size to the nanoscale (Fang et al., 2017; Shi et al., 2017). If the desired PBA crystal can provide large active areas for the nanogold loading, the enzymatic reaction signal will be remarkably

* Corresponding authors.
E-mail addresses: zychu@njtech.edu.cn (Z. Chu), wqjin@njtech.edu.cn (W. Jin).

https://doi.org/10.1016/j.bios.2018.09.094
Received 7 August 2018; Received in revised form 27 September 2018; Accepted 27 September 2018
Available online 28 September 2018
0956-5663/

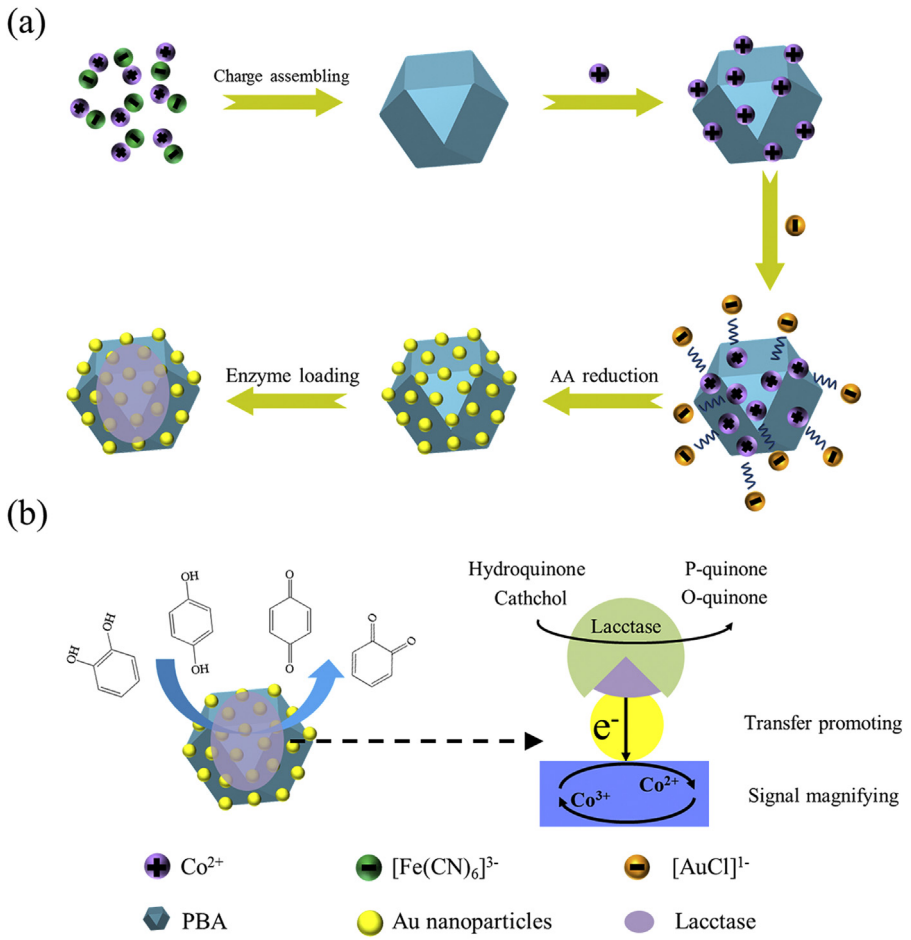

Fig. 1. (A) Schematic illustrating preparation process of the truncated cube-shaped Au/PBA nanocomposites; (B) Schematic illustration of the Au/PBA nanocomposites based phenolic biosensors for the detection of catechol and hydroquinone.

promoted to show a superior biosensing performance.

Herein, a novel phenolic biosensor for the trace analysis determination of catechol and hydroquinone was fabricated *via* the construction of a truncated cube-shaped Au/PBA nanocomposites prepared by a simple charge-assembly strategy. As shown in Fig. 1a, relied on the charge attractions among $[Fe(CN)_6]^{3-}$, Co^{2+}, and $[AuCl_4]^{3-}$ reactants, dense 10 nm Au particles can be directly synthesized to cover all fourteen faces of the PBA truncated nanocubes. Owing to the high surface area of each PBA crystal, abundant gold nanoparticles can bridge between the enzyme center and the PBA crystal for remarkably promoting the electron transfer (Fig. 1b), then the gathered current signals can be magnified through the redox process of the PBA. Due to the synergetic effects of above composited nanomaterials, the as-prepared phenolic biosensor can achieve a simultaneous test for the trace catechol and hydroquinone at different working potentials with rare interference signal, as well as a high sensitivity, an excellent linear range and a low detection limit.

2. Experiments

2.1. Reagents and apparatus

Potassium ferricyanide ($K_3Fe(CN)_6$), Cobalt(II) chloride ($CoCl_2$), and laccase (EC 420–150-4, ≥50 units/mg, from Rhus vernicifera) were purchased from Sigma-Aldrich company. Glutaraldehyde 25% (v/v) were obtained from Shanghai Lingfeng Chemical Reagent Co., Ltd. (China). Hydroquinone (HQ), catechol (CC), resorcinol (RC), phenol, uric acid (UA) and ascorbic acid (AA) were received from Sinopharm Chemical Reagent Co., Ltd. (China).

Field emission scanning electron microscope (FESEM, Hitachi, S-4800II) and transmission electron microscopy (TEM, JEOL JEM-2010 UHR) were applied to observe the surface morphology of the synthesized materials. X-ray diffractometer (D/MAX 2500 V/PC) with a Cu-Ka radiation (0.15419 nm), Fourier-transform infrared (FTIR) (Thermo Electron, Nicolet-8700, USA) and Raman spectrometer (Horiba Labram HR800, Japan) were respectively employed to measure the characteristic peaks and characteristic groups of $Co_3[Fe(CN)_6]_2$ and $Au/Co_3[Fe(CN)_6]_2$. X-ray photoelectron spectrometer (ESCALABMKLL) was utilized to analyze X-Ray photoelectron spectrometrys (XPS) and elements valence state.

2.2. Morphology control and synthesis of $Co_3[Fe(CN)_6]_2$

Firstly, 0.01 M $CoCl_2$ and 0.01 M $K_3Fe(CN)_6$ were prepared as reactants. Next, the morphology control of the product $Co_3[Fe(CN)_6]_2$ (CoFe) was carried out by adjust the synthesis time of chemical reaction with a low reaction rate. The synthesis time of 5, 40 and 80 min were respectively selected to observe the crystal growth.

2.3. Preparation of $Au/Co_3[Fe(CN)_6]_2$

Different volumes of 0.01 M $HAuCl_4$ were mixed into the above 20 mL $Co_3[Fe(CN)_6]_2$ suspension to adjust gold nanoparticles amount. After enough time to stir, 0.01 M ascorbic acid was used to reduce $HAuCl_4$ with a low injection rate. After the reaction finished, the hybrid solution was required to centrifuge with deionized water and ethanol

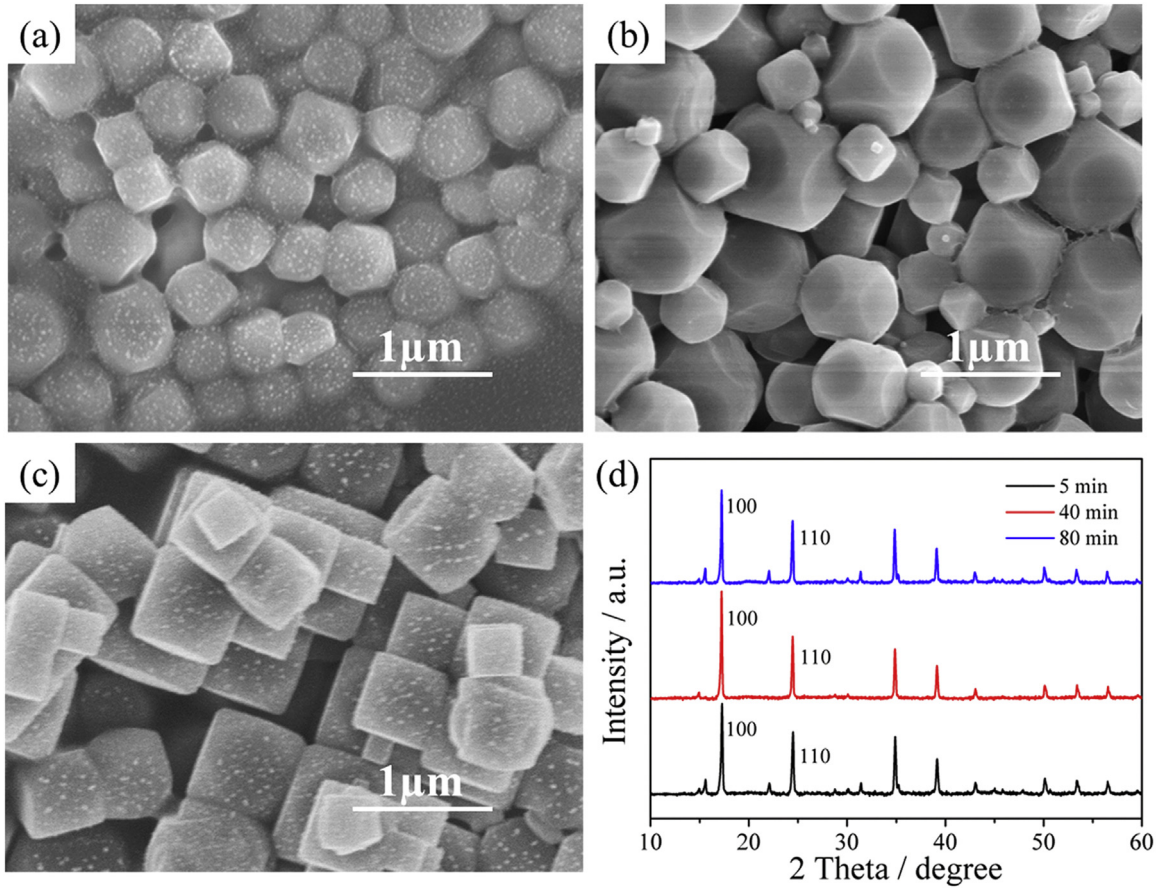

Fig. 2. Nanostructure evaluation of the PBA crystals at the synthesis time of 5 min (a), 40 min (b) and 80 min (c). (d) The XRD patterns of the as-prepared PBA crystals at different synthesis time.

each three times. The obtained product was dried at 60 °C.

2.4. Construction of the Au/$Co_3[Fe(CN)_6]_2$ based phenolic biosensors

20 mg Au/$Co_3[Fe(CN)_6]_2$ powder was mixed into 10 mL deionized water and stirred homogenously. 5 μL the prepared solution was dropped on the Au electrode surface. 100 U laccase was dissolved in 1 mL deionized water, and then 1.25% wt glutaraldehyde was added to crosslink enzyme. Next, 10 μL enzyme solution was dropped on the Au/$Co_3[Fe(CN)_6]_2$ modified electrode.

2.5. Electrochemical measurement

Electrochemical workstation (CHI 660E, Shanghai Chenhua Instrument Co. Ltd., China) was used to perform all electrochemical characterizations. The cyclic voltammetry (CV), differential pulse voltammetry (DPV) and chronoamperometry tests were operated in a 0.05 M phosphate buffer solution (PBS, pH 6.5) containing 0.1 M KCl. For CV scanning, the working type was set to the normal mode with the scan rate of 50 mV•s^{-1}. All CVs in the figures were the first scanning results. For the DPV experiments, the increment E was 0.004 V with the 0.05 V modulation amplitude, and the sampling width is 0.02 s. Electrochemical impedance spectroscopy (EIS) was operated in the indicator solution of 5 mmol L^{-1} $[Fe(CN)_6]^{4-/3-}$ (1:1) containing 0.1 M KCl with a frequency range from 0.1 Hz to 1000 kHz, and the initial test voltage and amplitude were set to 0 V and 5 mV, respectively. An Ag/AgCl (saturated KCl) electrode, a Pt wire and a gold disk electrode (diameter: 2 mm) were used as the reference electrode, counter electrode and working electrode, respectively.

3. Results and discussions

3.1. Nanostructure evolution of the Au/PBA nanocomposites

As our design in Fig. 1, the charge-assembly method is relied on the charge interaction between the reactant ions for crystallization. With the purpose to provide large active areas to attract free $[AuCl_4]^-$ for the gold growth, the geometric shape of the PBA crystal is desired to possess more faces. In our previous works, the well-defined PB nanocubes with six faces have been successfully synthesized by various control methods (Jiang et al., 2016; Yang et al., 2017; Chu et al., 2013, 2011). However, more geometric faces are still a challenge due to the difficulty in the exact control during crystal growth. Consequently, we carefully investigated the PBA morphology evolution during its whole crystallization period. At the initial growth stage, PBA crystals preferred to rapidly form a cube-like morphology with 300 nm. The defects appeared at the eight vertices of each crystal, showing round corners. Further prolonging the reaction time, these defect areas extended to generate several new faces which formed a truncated cubic shape. As a result, each PBA crystal totally possesses fourteen smooth geometric faces. However, allowing its continuous growth for more time would eliminate the new-born eight faces, returning to the initial nanocubes. This crystallization process can be surmised from the XRD results of above three growth stages. In Fig. 2d, among all typical peaks of PBA, (100) and (110) crystal faces changed most. The relative intensity ratios of the (100)/(110) reflections of CoFe PBA crystals prepared at 5 min, 40 min and 80 min were respectively calculated as 1.48, 1.76 and 1.49, indicating that the preferential orientation growth in the (100) direction determined the defect formation and extension to achieve the extra eight geometric faces (Liu et al., 2009; Shi et al., 2015).

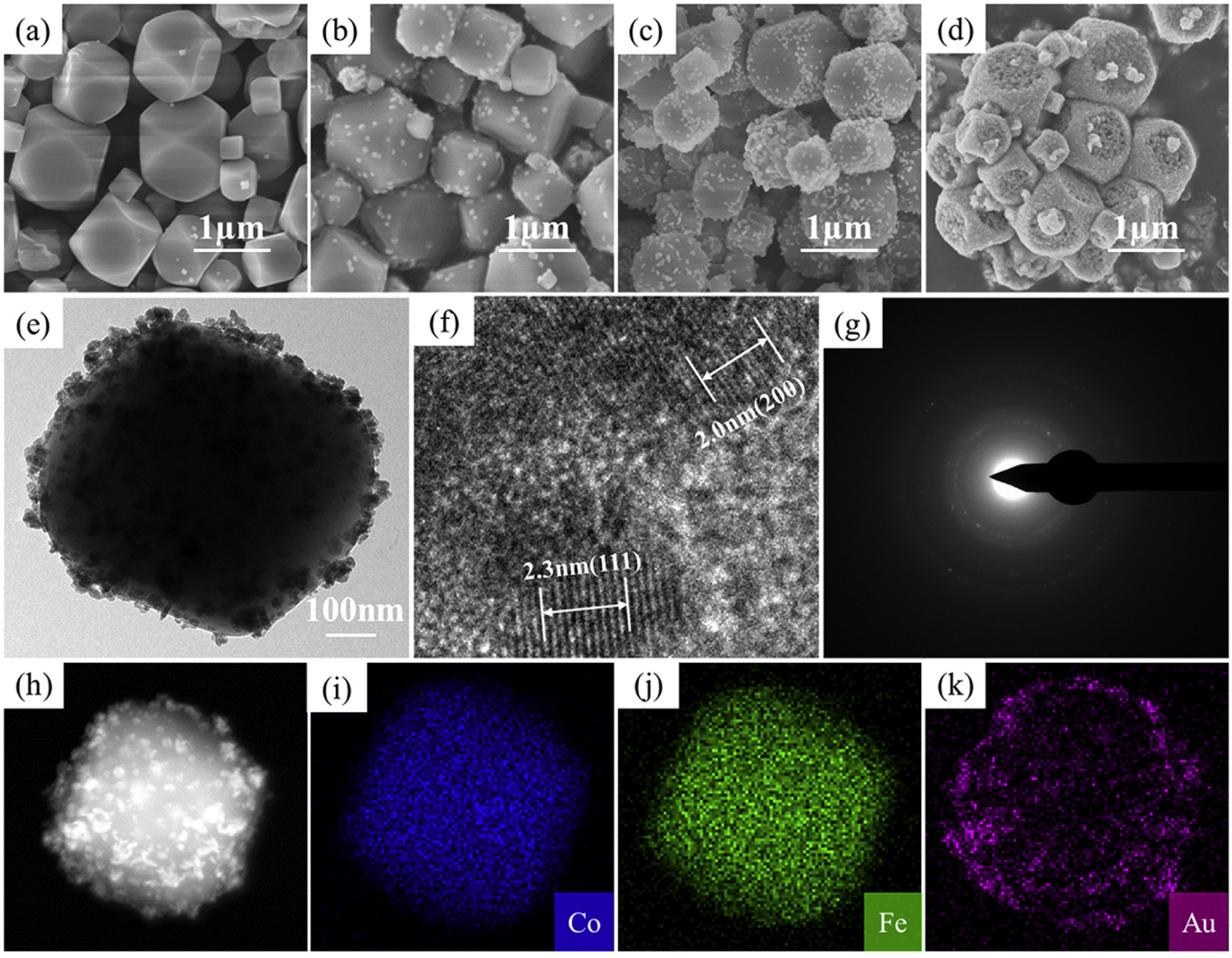

Fig. 3. FESEM images of Au/PBA nanocomposites prepared by reducing different $HAuCl_4$ concentrations (a: 0 mM, b: 1 mM, c: 3 mM, d: 5 mM); (e-f) TEM and HRTEM images of the Au/CoFe PBA nanocomposites; (f) SAED pattern of the Au/PBA nanocomposites; (h-k) The mapping results for three characteristic elements (Co, Fe and Au).

To sufficiently utilize the fourteen faces of PBA, gold nanoparticles are required to realize the *in-situ* growth on the each face. After finishing the PBA synthesis, the excess Co^{2+} reactant was added to produce positive charge sites surrounding all faces (Fig. S1) for the $[AuCl_4]^-$ attraction. Using this strategy, Au nanoparticles were able to gradually grow on the PBA crystal surface with the increase of the $HAuCl_4$ concentration (Fig. 3a to d). Till reaching to 5 mM $HAuCl_4$, each face was almost completely covered. More details could be obtained from the TEM characterization. As revealed in Fig. 3e, the interplanar spacing of Au nanoparticles on the PBA surface (Fig. 3f) was measured by lattice fringe and the values were calculated as approximately 0.23 nm and 0.2 nm, which respectively correspond to the 111 and 200 planes of Au. It was also in accord with the conclusion from the following XRD results (Fig. 4a) for the crystalline planes. The well-defined diffraction pattern in Fig. 3g indicated the polycrystalline nature of this nanocomposites. Besides, it is worthwhile mentioning that the Au element (Fig. 3h to k) was uniformly distributed on all faces of the PBA due to the effects of the positive charge.

Fig. 4a showed the XRD spectra of the above samples in Fig. 3a to d. The peaks located at 17.3∘, 24.2∘ and 35.2∘ respectively indicate the PBA crystalline plane of (200), (220) and (400). These peaks were well consistent with the standard X-ray diffraction pattern of $Co_3[Fe(CN)_6]_2$ (JCPDS 46–0907) (Bui et al., 2016). The two strongest peaks at 38.2∘ and 44.4∘ showed the (111) and (200) planes of Au (Shi et al., 2017; Balakumar and Prakash, 2015). This is due to the entire coverage of Au nanoparticles on the PBA surfaces to show much stronger response during the X-ray scanning. FTIR and Raman spectroscopy were also applied to further investigate the functional group composition of this nanocomposite. As observed in Fig. 4b, before and after depositing Au nanoparticles, the nanomaterial all exhibited a strong absorption peak at 2090 cm^{-1} which belonged to the CN- stretching absorption band of the PBA structure (Jiang et al., 2016; Zhang et al., 2018). Similarly in Fig. S2, the Raman specific peak at 2150 cm^{-1} was attributed to the CN- stretching vibration of PBA (Ariane et al., 2018). These evidences proved that the synthesized PBA crystal can maintain its cell structure during the Au formation.

The nanocomposite was examined by the XPS measurement to confirm its chemical compositions before and after the Au deposition. The survey spectra of the prepared $Co_3[Fe(CN)_6]_2$ and $Au/Co_3[Fe(CN)_6]_2$ (Fig. S3) indicated that this material was mainly composed of C, N, Fe, Co and Au elements. Fig. 4c exhibited that two main Co 2p peaks located at 781.9 eV (2p 3/2) and 797.8 eV (2p 1/2), representing the existence of Co^{2+}. Besides, the oxidation state of cobalt remained unaltered after the growth of Au nanoparticles, indicating the rare valance influence produced from Au nanoparticles. The Fe 2p spectra in Fig. 3d was composed by the characteristic peaks of Fe^{2+} and Fe^{3+}

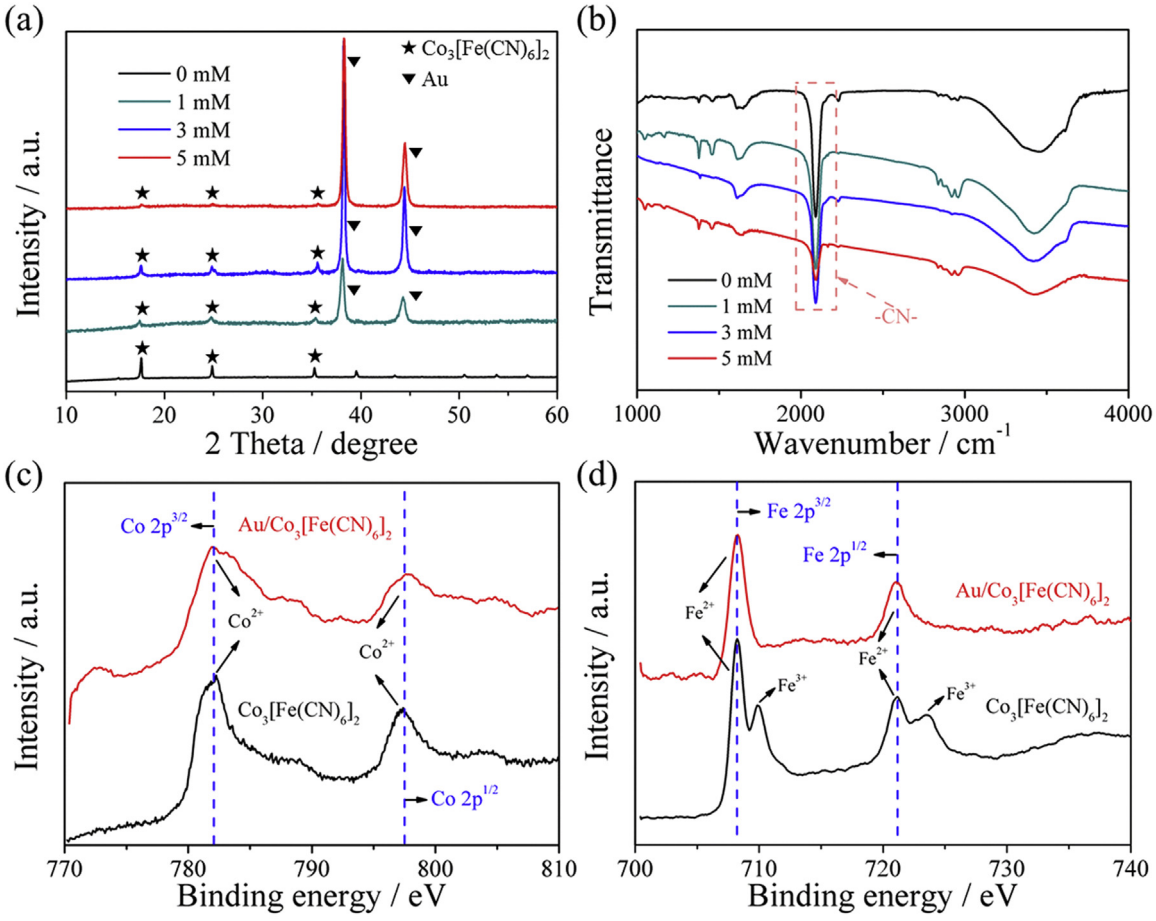

Fig. 4. (a-b) are respectively XRD patterns and FTIR spectra of Au/CoFe PBA nanocomposites fabricated at different Au concentrations (0, 1, 3 and 5 mM); (c-d) are respectively the XPS spectra of Co 2p and Fe 2p.

(Fe^{2+} $2p_{3/2}$ peak at 720.9 eV, Fe^{2+} $2p_{1/2}$ peak at 708.2 eV, Fe^{3+} $2p_{3/2}$ peak at 723.6 eV, Fe^{3+} $2p_{1/2}$ peak at 710.0 eV) (Castan et al., 2017; Zhang et al., 2010). The presence of Fe^{2+} may be ascribed to the electron transfer in the cell structure. However, the two Fe^{3+} characteristic peaks disappeared after the Au formation. This result is attributed to the excess AA injection for the $[AuCl_4]^-$ reduction, simultaneously reducing $[Fe(CN)_6]^{3-}$ to $[Fe(CN)_6]^{4-}$. Furthermore, the Au 4f peaks located at 83.7 eV and 87.4 eV in Fig. S4 demonstrate that the synthesized Au nanoparticles are of an elementary state (Minju et al., 2015).

3.2. Electrochemical behaviors of the fabricated electrodes

As designed, the introduction of Au nanoparticles is proposed to construct a high-speed channel for facilitating the electron transfer from the enzyme active center to the electrode surface. For confirming its effect, the prepared nanocomposites were modified on the gold electrodes for the EIS characterization. As shown in Fig. 5a, accompanying with the increase of the Au nanoparticle amount, the R_{ct} value was decreasing from 283 to 145 Ω. The result demonstrates that the coverage of Au nanoparticles can obviously promote the conductivity of the PBA crystals, benefiting the signal magnification. We also tested the CV performances of the bare, PBA and Au/PBA modified electrodes in a same indicator solution (10 mM $[Fe(CN)_6]^{3-}/[Fe(CN)_6]^{4-}$) to character their electrocatalytic activities (Fig. 5b). Compared to the bare electrode, the only PBA material modified electrode showed the weakened peak currents due to its unsatisfactory conductivity. However, a sudden enhancement of the redox currents happened after the Au deposition, indicating its great promotion as a high-speed highway for the electron transfer during the redox process. The effective specific surface area of Au/PBA modified electrodes could be calculated according to the below Randles-Sevcik equation:

$$\frac{I_p}{v^{1/2}} = (2.69* \quad 10^5) n^{3/2} D_0^{1/2} C_0^* A \tag{1}$$

Among this equation, I_p is the peak current, v is the scan rate, n is the number of electrons transferred in this redox process, D_0 is the diffusion coefficient of the molecules, C_0 is the concentration of the probe molecules and A is the specific surface area. Due to the fact that n, D_0 and C_0 in this equation are constant values, $I_p/v^{1/2}$ is proportional to the surface area (A). Therefore, it could be obtained that the effective surface area of the as-prepared electrode was 0.0821 ± 0.004 cm^2 from the Fig. S5 and Table S1.

An optimal working potential of the as-prepared biosensor was determined by DPV and CV measurements after the laccase was immobilized. Fig. 5c showed the potential scanning results of CC and HQ, respectively. Continuous injection of CC from 0 to 30 μM, an increasing oxidation peak current appeared at 170 mV. Similarly, an oxidation peak of HQ was generated at 70 mV. Hence, the two isomers possessed the different characteristic oxidation potentials for the Au/PBA nanocomposite. This difference is mainly attributed to the distinct molecular structures of CC and HQ. The duel phenolic hydroxyl groups of HQ locate at the para-position with much lower steric effect than ortho-position to contact the laccase for the easier oxidation. In this case, it is promising to realize a simultaneous recognition of CC and HQ and the possibility was confirmed from the results in Fig. 5d. CC and HQ with a same concentration were together injected for the CV scanning. It can be found that two obvious pairs of redox peaks, respectively belonging

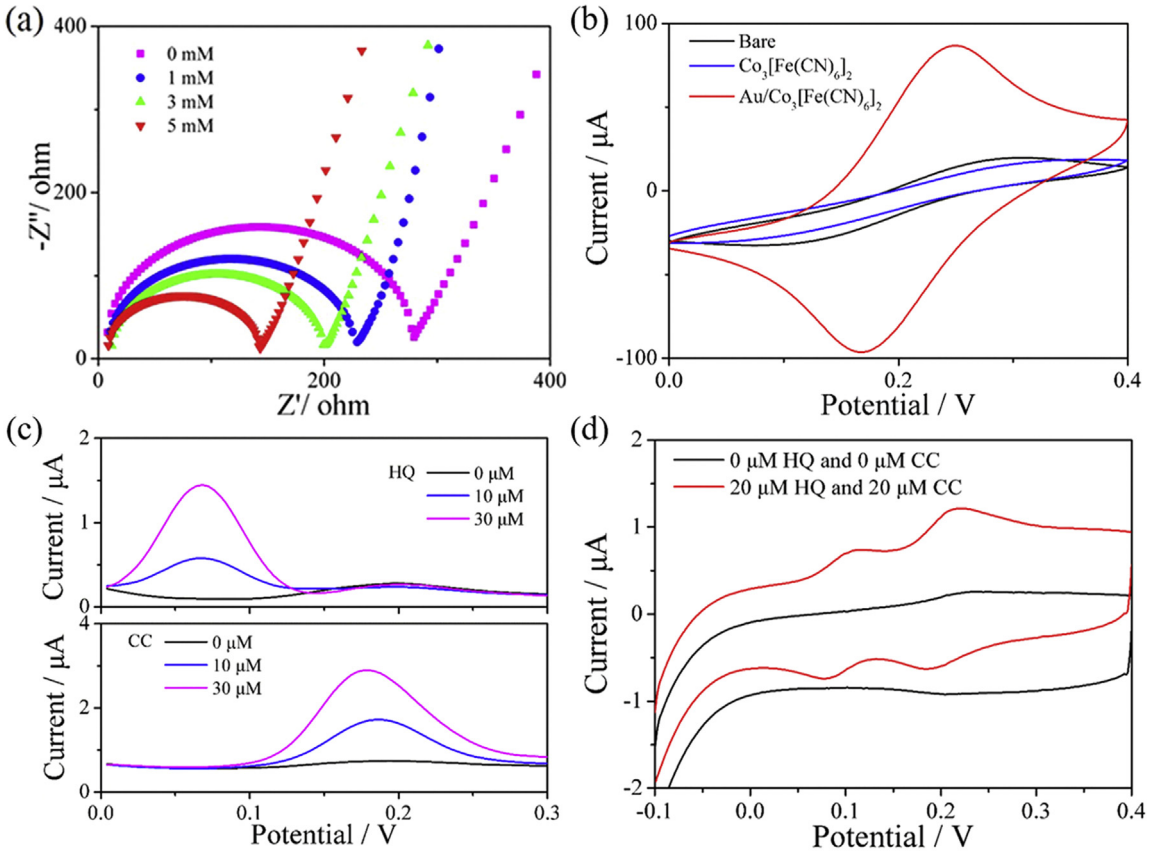

Fig. 5. EIS behaviors of the as-prepare biosensors based on different Au nanoparticles contents in presence of 5 mM $[Fe(CN)_6]^{3-/4-}$ solution containing 0.1 M KCl; (b) CV behaviors of the bare, PBA, Au/ PBA modified electrodes in presence of 10 mM $[Fe(CN)_6]^{3-/4}$ containing 0.1 M KCl at a scan rate of 50 mVs^{-1}. (c) DPV responses of the as-prepare biosensors for CC and HQ in 0.05 M PBS; (d) CV responses of the as-prepare biosensors for CC and HQ DPV responses of the as-prepare biosensors for CC and HQ in 0.05 M PBS.

to CC and HQ. It was worth mentioning that there were no obvious mutual interference for the response current and potential displayed in this diagram. Moreover, the electrochemical control procedure of the as-prepared biosensor for the simultaneous detections of HQ and CC was further discussed through investigating the change of peak currents with increasing the scanning rates during the CV characterization. As shown in Fig. S6a, both of the CC and HQ redox currents were enhanced with the continuous increase of the scanning rates. Combining with the calibration cures of Fig. S6b, it could be found that their peak currents were proportional to the square root of scanning rates. The linear relationships demonstrated that the simultaneous electrochemical oxidation of CC and HQ was a diffusion-controlled process (Jiang et al., 2018; Cinti et al., 2014)." Therefore, the as-prepared biosensor is qualified to be applied in the quantitative analysis of CC and HQ.

For reliably testing the independence of CC and HQ during the electrochemical detection, different concentrations of CC and HQ were together existed for the DPV scanning. Fig. 6a showed the relationship between the DPV current responses and the CC concentrations in the presence of 10 μM HQ. Apparently, the initial HQ injection could arouse an obvious peak at 70 mV and the peak currents at 170 mV gradually raised after the subsequent injection of every 10 μM CC. It is worthy emphasizing that the HQ peak current value rarely changed with the CC concentration increasing, demonstrating the rare interference produced from HQ for the CC detection. The same phenomenon can be observed in the Fig. 6b with the change of the HQ concentration in a fixed CC concentration. The above two results indicated the mutual independence and anti-interference between the CC and HQ by using our prepared biosensor. Each testing was repeated to three times to study the performance errors. According to the data from Fig. 6a and b, the sensitivities were respectively calculated as 62.5 ± 2.1 μA•mM^{-1} (CC) and 44.9 ± 1.8 μA•mM^{-1} (HQ). Subsequently, each 10 μM CC and HQ were simultaneously injected into the same detection system to investigate their sensitivities. Showing from the Fig. 6c and d, the peak currents of CC and HQ can follow the linear relationships with their concentrations, deriving the sensitivities of 62.0 ± 1.9 μA•mM^{-1} (CC) and 38.4 ± 1.4 μA•mM^{-1} (HQ). There were rare sensitivity differences between the single and both concentration changes for the each target. In order to exhibit the advances of our prepared biosensor, we had compared its performance with those in the other reports. As shown in Table S2, the as-prepared biosensor was of the remarkable advantages in the linear range (CC: 0.2–550 μM, HQ: 1–550 μM) and detection limit (CC:0.06 ± 0.001 μM, HQ:0.3 ± 0.007 μM) attributed to the excellent conductivity and electrocatalysis from our designed Au/PBA nanocomposite.

3.3. Selectivity, reproducibility and stability of the as-prepared biosensor

Selectivity is a vital parameter to evaluate the overall performance of biosensors. Therefore, the common interfering substances, such as RC, PE, UA and AA, were selected to investigate the selectivity of the as-prepared biosensor. Chronoamperometry results in Fig. S7a and b indicated that, with the successive additions of various interfering substances, no obvious current variations were produced during the detections of CC or HQ. When CC or HQ was added again, this biosensor can still provide a strong and fast current response. Above results could demonstrate that our prepared biosensor can only recognize the CC and HQ at their certain active potentials with a good selectivity.

With the purpose to test the reproducibility and long-term stability

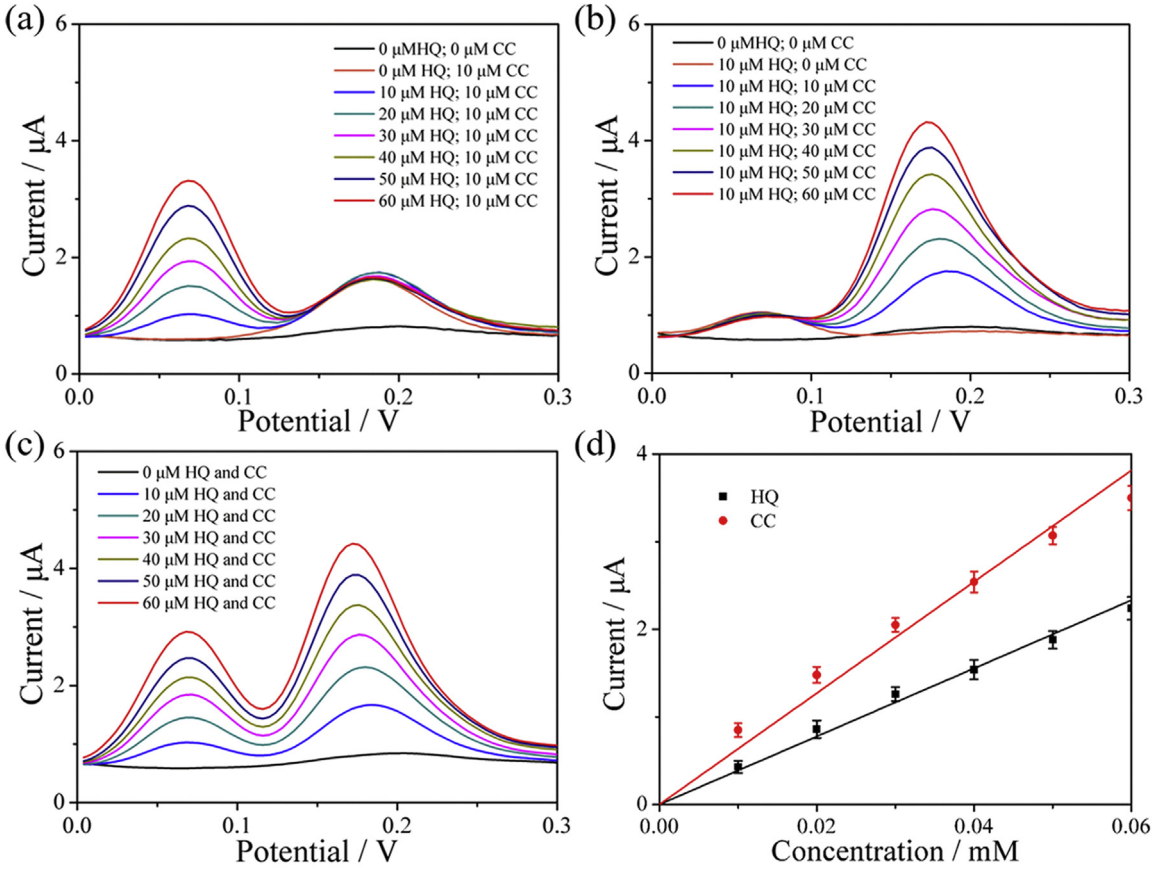

Fig. 6. (a) DPVs of Au/PBA based electrodes in the presence of 10 μM HQ with different CC concentrations (10–60 μM); (b) DPVs of Au/PBA based electrodes in the presence of 10 μM CC with different HQ concentrations (10–60 μM); (c) DPVs of Au/PBA based electrodes in the presence of binary mixture of CC and HQ (10–60 μM); (d) Linear calibration curves for the current response of CC and HQ (c). The RSD for CC and HQ were respectively calculated as 5.52% and 6.23%.

of the phenolic biosensors, 5 independent electrodes were fabricated under the same conditions and CC was selected as a target. The sensitivity is obtained through the DPV measurement with the successive addition of 10 μM CC. The relative standard deviation (RSD) was tested as 5.52% to show its excellent reproducibility. In addition, the long-term stability can be obtained by storing one electrode at 4 °C with the continuous examinations for every five days. After one month usage, this biosensor can still keep 86% initial sensitivity, indicating the outstanding usage stability.

4. Conclusion

We have successfully designed a truncated cube-shaped Au/PBA nanocomposite based phenolic biosensor for the simultaneous and sensitive detection of CC and HQ. The multifaceted geometry is beneficial for the simultaneous increase of Au loading area and PBA catalytic sites, resulting in a synergetic promotion of the conductivity and electrocatalysis. The as-prepared biosensor exhibits an extreme wide linear range and an ultralow detection limit. The preparation strategy of PBA is of practical significance for the crystal regulation of other PBAs. However, the accuracy of the fabricated phenolic biosensor remains to be examined when it involves a complex practical system.

Acknowledgements

This work was financially supported by National Natural Science Foundation of China (Nos. 21727818 and 21706116), the Innovative Research Team Program by the Ministry of Education of China (No.IRT_17R54), the Top-notch Academic Programs Project of Jiangsu Higher Education Institutions (TAPP) and the Priority Academic Program Development of Jiangsu Higher Education Institutions (PAPD).

Appendix A. Supporting information

Supplementary data associated with this article can be found in the online version at doi:10.1016/j.bios.2018.09.094.

References

Arduini, F., Zanardi, C., Cinti, S., Terzi, F., Moscone, D., Palleschi, G., Seebe, R., 2015. Sens. Actuators B Chem. 212, 536–543.
Ariane, S., Samantha, H., Aldo, J.G.Z., 2018. J. Electroanal. Chem. 22, 2003–2012.
Balakumar, V., Prakash, P., 2015. Sens. Actuators B Chem. 253, 392–399.
Bensalah, G., Cañizares, P., Sáez, C., Lobato, J., Rodrigo, M.A., 2005. Environ. Sci. Technol. 39, 7234.
Bui, H.T., Ahn, D.Y., Shrestha, N.K., Sung, M.M., Lee, J.K., Han, S.-H., 2016. J. Mater. Chem. A 4, 9781–9788.
Castan, A., Forel, S.L., Catala, Florea, I., Fossard, F., Bouanis, F., Andrieux-Ledier, A., Mazerat, S., Mallah, T., Huc, V., Loiseau, A., Cojocaru, C.S., 2017. Carbon 123, 583–592.
Chao, L., Wang, W., Dai, M.Z., Ma, Y.X., Sun, L.G., Qin, X.L., Xie, Q.J., 2016. J. Electroanal. Chem. 778, 66–73.
Chu, Z.Y., Shi, L., Zhang, Y.N., Jin, W.Q., Xu, N.P., 2011. J. Mater. Chem. 21, 11968–11972.
Chu, Z.Y., Shi, L., Liu, Y., Jin, W.Q., Xu, N.P., 2013. Biosens. Bioelectron. 47, 329–334.
Chu, Z.Y., Liu, Y., Jin, W.Q., 2017. Biosens. Bioelectron. 96, 17–25.
Cinti, S., Arduini, F., Moscone, D., Palleschi, G., Killard, A.J., 2014. Sensors 14, 14222–14234.
Fang, X., Liu, J.F., Wang, J., Zhao, H., Ren, H.X., Li, Z.X., 2017. Biosens. Bioelectron. 97, 218–225.
Figueiredo, E.C., Tarley, C.R.T., Kubota, L.T., Rath, S., Arruda, M.A.Z., 2007. Microchem. J. 85, 290–296.
Freire, R.S., Duran, N., Kubota, L.T., 2002. Electrochemical biosensor-based devices for continuous phenols monitoring in environmental matrices. J. Braz. Chem. Soc. 13, 456–462.

Hitoshi, M., Hisanori, I., Hiroki, H., Atsunori, H., Hirotaka, U., 2017. ACS Catal. 7, 725–734.
Ho, K.-C., Chen, C.-Y., Hsu, H.C., Chen, L.C., Shiesh, S.-C., Lin, X.-Z., 2004. Biosens. Bioelectron. 20, 3–8.
Jiang, D.F., Chu, Z.Y., Peng, J.M., Jin, W.Q., 2016. Sens. Actuators B Chem. 228, 679–687.
Jiang, D.F., Li, C.P., Liu, T., Li, L.L., Chu, Z.Y., Jin, W.Q., Ren, X.M., 2017. Sens. Actuator B Chem. 241, 860–867.
Jiang, D.F., Chu, Z.Y., Peng, J.M., Luo, J.Y., Mao, Y.Y., Yang, P.Q., Jin, W.Q., 2018. Electrochim. Acta 270, 147–155.
Kaisheva, A., Iliev, I., Kazareva, R., Christov, S., Wollenberger, U., Scheller, F., 1996. Sens. Actuators B Chem. 3, 39–43.
Kanamori, T., Funatsu, T., Tsunoda, M., 2016. Analyst 141, 2568–2573.
Karim, M.N., Lee, J.E., Lee, H.J., 2014. Biosens. Bioelectron. 61, 147–151.
Liu, Z., Wen, X.D., Wu, X.L., Gao, Y.J., Chen, H.T., Zhu, J., Chu, P.K., 2009. J. Am. Chem. Soc. 131, 9405–9412 9.
Lv, M., Wei, M., Rong, F., Terashima, C., Fujishima, A., Gu, Z.-Z., 2010. Electroanalysis 22, 199–203.
Mattos, I.L., Gorton, L., 2001. Quim. Nova 24, 200–205.
Melissa, M.R.-D., Gibrán, S.A.-N., José, M.R.-D., Graciano, D.-A., Sergio, O.M.-C., Damià, B., Roberto, P., 2015. Trends Anal. Chem. 74, 21–45.
Minju, K., Young, K., Sang, K., Soonhyun, K., 2015. In, Su-Il. Appl. Catal. B-Environ. 166, 423–431.
Qaisar, A., Samuel, B.A., 2009. Development of a potentiometric catechol biosensor by entrapment of tyrosinase within polypyrrole film. Sens. Actuators B Chem. 140, 5–11.
Selvakumar, P., Sayee, K.R., Chen, S.-M., Thomas, C.K.Y., Pan, Y.F., Tse-Wei, Chen, Vijayalakshmi, V., Sonadevi, S., 2017. Sci. Rep. 7, 41214.
Shi, L., Chu, Z., Liu, Y., Jin, W., 2015. J. Mater. Chem. B 3, 3134–3140.
Shi, L., Wang, Y., Ding, S.M., Chu, Z.Y., Yin, Y., Jiang, D.F., Luo, J.Y., Jin, W.Q., 2017. Biosens. Bioelectron. 89, 871–879.
Svitel, J., Miertus, S., 1998. Development of tyrosinase-based biosensor and its application for monitoring of bioremediation of phenol and phenolic compounds. Environ. Sci. Technol. 32, 828–832.
Wang, Z., Li, S., Lv, Q., 2007. Sens. Actuators B Chem. 127, 420–425.
Wohlfahrt, G., Witt, S., Hendle, J., Schomburg, D., Kalisz, H.M., Hecht, H.-J., Acta Crystallogr, Sect, D., 1999. Biol. Crystallogr. 55, 969–977.
Yang, P.Q., Peng, J.M., Chu, Z.Y., Jiang, D.F., Jin, W.Q., 2017. Biosens. Bioelectron. 92, 709–717.
Zhang, X.J., He, P., Zhang, X.Q., Li, C.X., Liu, H.H., Wang, S., Dong, F.Q., 2018. Electrochim. Acta 276, 92–101.
Zhang, X.Q., Gong, S.W., Zhang, Y., Yang, T., Wang, C.-Y., Gu, N., 2010. J. Mater. Chem. 20, 5110–5116.